

High Efficiency Cu(In,Ga)Se₂ Flexible Solar Cells Fabricated by Roll-to-Roll Metallic Precursor Co-sputtering Method

Rui Zhang¹, Dennis R. Hollars², and Jerzy Kanicki^{1*}

¹Solid State Electronic Laboratory, Department of Electrical Engineering and Computer Science, University of Michigan, Ann Arbor, MI 48109, U.S.A.

²NuvoSun Inc., Milpitas, CA 95035, U.S.A.

E-mail: kanicki@umich.edu

Received November 5, 2012; accepted June 19, 2013; published online August 23, 2013

We report on a Cu(In,Ga)Se₂ (CIGS) solar cell fabricated on flexible stainless steel substrate by a low cost mass production roll-to-roll process. Fabricated device has a high energy conversion efficiency of 14%, with short circuit current density (J_{sc}) of 36.6 mA cm⁻² and open circuit voltage (V_{oc}) of 0.55 V. A two-dimensional (2D) simulation model for CIGS solar cell design and optimization was proposed. Opto-electrical properties showed that both experimental and simulated results are consistent with each other. The photons absorber in CIGS solar cells was prepared by co-sputtering metallic precursors of In and CuGa followed by thermal annealing in Se vapor. The device chemical properties were analyzed by secondary ion mass spectrometry (SIMS) and transmission/scan electron microscopy (TEM/SEM). Indium and gallium interdiffusions were observed during the growth of film, forming a band grading in CIGS layer. Accumulation of In at the top CIGS surface, resulting in a low bandgap, was responsible for the limited output open circuit voltage. Nano-scale voids were observed in the grown CIGS layer. A model based on Kirkendall effect and interdiffusion of atoms during selenization is developed to explain the formation mechanism of these voids. Na and K incorporation as well as metallic impurities diffusion are also discussed. © 2013 The Japan Society of Applied Physics

1. Introduction

Renewable energy technology has been gaining more and more interests as being considered as a possible approach to solve many modern society issues: such as making up for reduced oil/gas resources, reducing fossil fuel induced air pollution and even developing economics in remote rural regions. Photovoltaic (PV) devices, that convert light photons into electricity, are expected to play an important role in future energy production.¹ Nowadays, silicon-based, including crystal silicon and polycrystalline silicon, solar cells have dominated the current PV market. However, several other new emerging technologies, based on thin-film,² dye-sensitized,³ and organic materials,⁴ are attracting attention of researchers. One of the most promising thin-film materials is polycrystalline chalcopyrite Cu(InGa)Se₂ (CIGS). It has been demonstrated by National Renewable Energy Laboratory (NREL) that CIGS solar cell can reach up to 20.3% energy conversion efficiency.⁵ Flexible substrates, compared with rigid glass substrates, enables implementation of roll-to-roll deposition methods which have potential to greatly reduce the fabrication cost, and to increase throughput. At the same time, reduction of the substrate weight and providing flexibility broaden the device application field. For example, flexible solar cell modules using stainless steel (SS) substrate can be integrated with curved roofs. Most investigated flexible substrates are polymer such as polyimide,^{6,7} and metal foils such as SS and titanium.⁸ In the past few years, several groups have reported on development of CIGS solar cell on flexible substrates. Kim et al.⁹ reported a flexible CIGS solar cell on SS substrate by co-evaporation process with efficiency of ~10.57%. Herrman et al.¹⁰ investigated barrier layers for flexible CIGS thin-film solar cells on metal foils. The device fabricated on titanium foil achieved external efficiency of about 13%. Rudmann et al.¹¹ and Caballo et al.¹² evaluated sodium incorporation strategies during CIGS growth. Most recently, researchers in EMPA of ETH Zurich, Chirila et al.,¹³ reported a 18.7% efficiency CIGS solar

cell fabricated on polyimide substrates by a high vacuum 4-elements co-evaporation method. This is the world highest record in efficiency for flexible solar cells. R&D engineers also made some progress in transferring these technologies from laboratory into industry. Matsushita claimed 17.0% efficiency CIGS solar cells on SS substrate in 2003.¹⁴ Global Solar Energy reported 11.3% efficiency on polyimide substrate and 13.2% efficiency on metal substrate.^{15,16} To produce CIGS thin film either (i) co-evaporation of elemental Cu, In, Ga, and Se in high vacuum, or (ii) deposition of bi-layer precursor on the back contact followed by selenization or sulfurization are used. Florida Solar Energy Center (FSEC)¹⁷ sputtered Cu–In–Ga tri-layers as a precursor and let them react in the H₂S:Ar gas environment, while International Solar Electric Technology (ISET)¹⁸ performed thermal annealing of CIGS in N₂:H₂Se mixed-gas environment. Klaer,¹⁹ from Hahn-Meitner Institute, used sputtering of Cu and In to form a bi-layer precursor followed by sulfurization and post-deposition CuS etching. Nanosolar used screen printing of CIGS nanoparticles as precursor followed by rapid thermal annealing. Miasole²⁰ instead performed selenization step during the rf-sputtering using a Se-atmosphere. Today, the best solar cell fabricated by co-evaporation method on flexible substrates has efficiency of ~18.7%. The reported efficiencies for devices fabricated by other methods are below 13%. We can speculate that co-evaporation process has a better control of CIGS elements composition during the thin film growth. However, each of these methods has its own disadvantages when implemented in mass production: (i) co-evaporation method requires sophisticated equipment which may not be suitable for large area substrates; (ii) H₂Se and H₂S are very toxic and only stable at normal room conditions, so that thermal high temperature annealing process in H₂Se and H₂S gas atmosphere can be dangerous; (iii) instead of using H₂Se and H₂S, sputtering of CIGS in Se vapor is safer approach but it is more difficult to control CIGS elements composition during film growth. To overcome these issues, we developed a modified roll-to-roll

precursor-selenization two-step process for fabrication of CIGS layer over SS flexible substrate. Computer-aid two-dimensional (2D) numerical simulation has been widely used for solar cell design and device structure optimization.^{21,22} It provides key insights into fundamental physics of solar cell operation, enabling engineers to explore full range of design alternatives. However, most of current simulation models have been developed only for traditional silicon based solar cells. Modeling of compound semiconductor based solar cells, namely Cadmium Telluride and Cu(In,Ga)Se₂, are still rare due to lack of full understanding of their physical models and material parameters. As the complexity of solar cell designs evolves over time, purely experimental approaches are no longer sufficient for device design and optimization. To build a useful simulation model for CIGS solar cell becomes an important and necessary task.

In this work, we proposed a 2D simulation model for CIGS solar cell based on simulator software APSYS and demonstrated that this software can be used for design of advanced CIGS solar cells. We then fabricated CIGS solar cells on flexible SS substrates using a modified two-step co-sputtering method. The device electronic properties were characterized by current density–voltage (*J*–*V*) and quantum efficiency (QE) experiments. Both simulation results and experimental measured data were compared and analyzed. Finally, secondary ion mass spectrometry (SIMS) and transmission/scan electron microscopy (TEM/SEM) were used to characterize device physicochemical properties.

2. Modeling and Experimental

2.1 Device simulation

In this work, 2D simulation of Cu(In,Ga)Se₂ solar cell was performed using software APSYS.²³ Complex trapping, recombination mechanism models have been taken into account in the simulation. The defect states are described as deep level donor or acceptor like traps. Impurity concentration (trap density) and the electrons/holes capture cross section are used to specify the trap states.²⁴ The minority carrier lifetime is then expressed as

$$\frac{1}{\tau_{n,p}} = v \times \sigma_c \times D_t, \quad (1)$$

where $\tau_{n,p}$ is minority carrier lifetime, v is thermal velocity, σ_c is capture cross section, and D_t is trap density. The device structure used in this simulation is, aluminum (Al)/aluminum doped zinc oxide (AZO)/intrinsic zinc oxide (i-ZnO)/cadmium sulfide (CdS)/CIGS/molybdenum (Mo), shown in Fig. 2 inset (a). The set of parameters needed for electrical and optical modeling was obtained from experimental data and literature.^{25,26} Typical parameter set is shown in Table I. All simulations are done under a standard air mass 1.5 global spectra (AM1.5G) solar irradiation.²⁷ Series resistance and shunt resistance obtained from measured *J*–*V* curves were also included in this simulation.

2.2 Device fabrication

Solar cells investigated in this work were fabricated as follows. A moving one meter wide and 50- μ m-thick SS web is used as the flexible substrate. The SS is first cleaned

Table I. Parameters set used for the modeling of CIGS solar cell.

	CIGS	CdS	Al:ZnO
Dielectric constant ϵ_r	13.6	8.9	8.5
Electron affinity χ_e (eV)	4.5	3.8	4.6
Band gap E_g (eV)	1.15	2.42	3.3
Electron mobility μ_n (cm ² V ⁻¹ s ⁻¹)	60	35	100
Hole mobility μ_h (cm ² V ⁻¹ s ⁻¹)	10	16	31
Electron lifetime τ_n (s)	10 ⁻⁸	10 ⁻⁹	10 ⁻⁸
Hole lifetime τ_p (s)	10 ⁻⁸	10 ⁻⁹	10 ⁻⁸
Real index n_{real}	2.6	2.4	2.0
Absorption α_0 (cm ⁻¹)	2.8×10^5	3.4×10^4	—

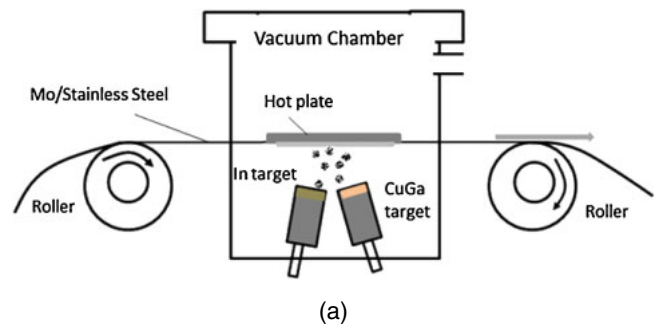


Fig. 1. (Color online) Schematic of CIGS co-sputtering system and roll-to-roll co-sputtering machine used in this work.

by ion etch prior to the deposition of a chromium layer by DC sputtering. A molybdenum film was then deposited on the top of Cr by DC sputtering as the back contact electrode. This step was repeated one more time to produce four layers Cr/Mo/Cr/Mo structure. The CIGS layer was prepared by a precursor-selenization two-step process. First, metallic precursors were deposited by co-sputtering of In and CuGa targets on the top of Mo surface. During co-sputtering process, the substrate was heated up to 250 °C and was moving in one direction. The sputtering targets were arranged such as moving substrate was first seeing In target before CuGa:In mixed phase was deposited. A schematic of precursor co-sputtering based roll-to-roll processing system is shown in Fig. 1(a). The resulting metallic stacked precursor has a structure composed of a very thin In layer followed by a indium–copper–gallium (InCuGa) matrix containing various indium islands located within bulk of the thin film, with the In largest concentration located near the top of the deposited film due to heating of the

substrate. The total film thickness of $\sim 700\text{--}900\text{ nm}$ and InCuGa film composition of $[\text{Cu}]/([\text{In}] + [\text{Ga}]) \sim 0.9$ is realized. The metallic stacked precursors were then annealed in selenium (Se) vapor at a higher temperature, around 550°C , for tens of minutes. The CIGS layer is formed after selenization step. Its thickness increased from initial thickness of ~ 900 to 1400 nm . Sodium (Na), necessary for sodium-free SS substrates, was introduced during the initial step of thin film preparation from evaporating sodium fluoride compound (NaF) on the top of the Mo surface. Figure 1(b) shows the schematic of sputtering system and equipment used. The stack was then coated with $\sim 100\text{-nm-thick}$ CdS buffer layer using chemical bath deposition (CBD). The structures were immersed in Cd^{2+} solution at $65\text{--}70^\circ\text{C}$ with stirring for $\sim 20\text{ min}$ to deposit CdS layer. At last, the Al-doped ZnO (AZO) bi-layer was deposited by AC sputtering. The AZO bi-layer has a thin resistive film between CdS and transparent conductive AZO produced by addition of oxygen (O_2) in the argon (Ar) atmosphere during initial AZO sputtering stage. The conductive AZO layer is used as transparent conductive electrode (TCO) in our CIGS solar cells. No antireflection (AR) coating was used in our device. Finally, single cells with different areas were defined by mechanical scribing.

2.3 Device evaluation

SIMS and SEM/TEM were performed to characterize quantitatively our device's physic-chemical properties. During SIMS analysis, the CIGS sample was sputtered with a beam of primary ions (Cs^+) at energies of 1 to 30 KeV. Primary ions were implanted and mixed with sample atoms to depth of 1 to 10 nm. Secondary ions formed during the sputtering process were extracted and analyzed using a high resolution mass spectrometer. The obtained material composition profiles were calibrated by Rutherford backscattering spectrometry (RBS) and Evans Analytical Group (EAG) reference clean CIGS samples. Point-by-point correction was used for the ion yield and sputter rate change as the matrix changes. In addition, the primary ion species, angle of impact, energy of impact, the secondary ion species selected for detection, data point density and the mass resolution have been considered in SIMS analysis protocol. For SEM/TEM, samples were prepared using a proprietary in-situ lift-out technique in a FEI focus ion beam (FIB) 200 lifting a section from the SS foil. The protective layers applied to the samples were as follows (from the sample surface up): a thin polymeric coating was applied locally on the sample then $\sim 75\text{--}100\text{ nm}$ of 99.99% purity Pt was applied by magnetron sputter coating and lastly a Pt/C capping layer was applied to the automated optical inspection (AOI) by the FIB in-situ. In addition, some samples were prepared by flaking the coating from a small piece of substrate to get a "cleave" edge. The samples were imaged in a Hitachi HD-2300 dedicated STEM/TEM operated at 200 kV having a nominal 0.20 nm diameter electron beam. To characterize electronic properties of devices, $J\text{--}V$ characteristics were measured under the standard test conditions (100 mW/cm^2 , 25°C , AM1.5G). External quantum efficiency versus wavelength curve was also measured. Devices performance variations under different light intensities were measured by

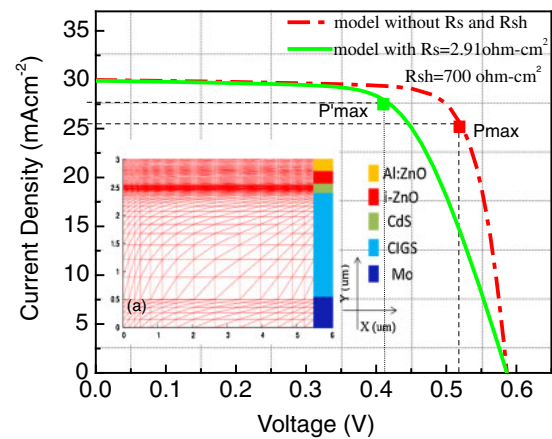


Fig. 2. (Color online) Simulated $J\text{--}V$ curves of the CIGS solar cell with and without series/shunt resistant: inset (a) shows mesh structure of the modeling device used in the simulation.

changing incident light using different filters, with transmittance ranging from 4 to 85%.

3. Results and Discussion

3.1 Simulation results

Per previous report,²⁸⁾ calculated band diagram of the investigated device in thermodynamic equilibrium (dark, zero-bias voltage) has a following structure: from the left is the back contact, $0.5\text{-}\mu\text{m-thick}$ Mo with electron affinity of 4.9 eV, coated with a $1.5\text{-}\mu\text{m-thick}$ chalcopyrite polycrystalline $\text{Cu}(\text{In}_{0.7}\text{Ga}_{0.3})\text{Se}_2$ absorber having an average bandgap energy of $\sim 1.15\text{ eV}$. The p-n hetero-junction is formed between p-type CIGS and n-type CdS buffer layer having a bandgap energy of $\sim 2.42\text{ eV}$. Band discontinuity on CIGS/CdS hetero-junction has a conduction band offset ΔE_c of $\sim 0.17\text{ eV}$ and a valance band offset ΔE_v of $\sim 1.44\text{ eV}$, where a notch is formed at CdS/CIGS interface due to difference of the electron affinity.^{29,30)} The front contact consists of a bilayer of intrinsic and Al-doped ZnO films having a wide bandgap of $\sim 3.3\text{ eV}$. The CIGS layer can be divided into space charge region (SCR) and quasi-neutral region (QNR). The simulation²⁸⁾ of the optical absorption distribution across the device showed that the absorbed optical energy decreases along light incident path. This decrease can be explained by considering the light absorption by ZnO and CdS layer, respectively. Reducing or/and optimizing the thickness of these layers could minimize these losses.²⁶⁾

Figure 2 shows the simulated $J\text{--}V$ curves for CIGS solar cell without series resistance (R_s) and shunt resistance (R_{SH}), and with $R_s = 2.91\ \Omega\text{ cm}^2$ and $R_{SH} = 700\ \Omega\text{ cm}^2$, respectively. In this work, solar cell without R_s and R_{SH} has following performance: external efficiency $\eta = 14.3\%$, open circuit voltage $V_{oc} = 0.58\text{ V}$, short circuit current density $J_{sc} = 30.0\text{ mA/cm}^2$, fill factor $FF = 0.84$ while device with the R_s and R_{SH} has performance as follow: $\eta = 12.1\%$, $V_{oc} = 0.58\text{ V}$, $J_{sc} = 29.4\text{ mA/cm}^2$, $FF = 0.71$. The R_s and R_{SH} is responsible for reduction of FF and solar cell external efficiency.

3.2 Opto-electrical characterization

The experimental $J\text{--}V$ and power density-voltage ($P\text{--}V$) characteristics measured under a standard 100 mW/cm^2 AM1.5 spectrum illumination at room temperature are

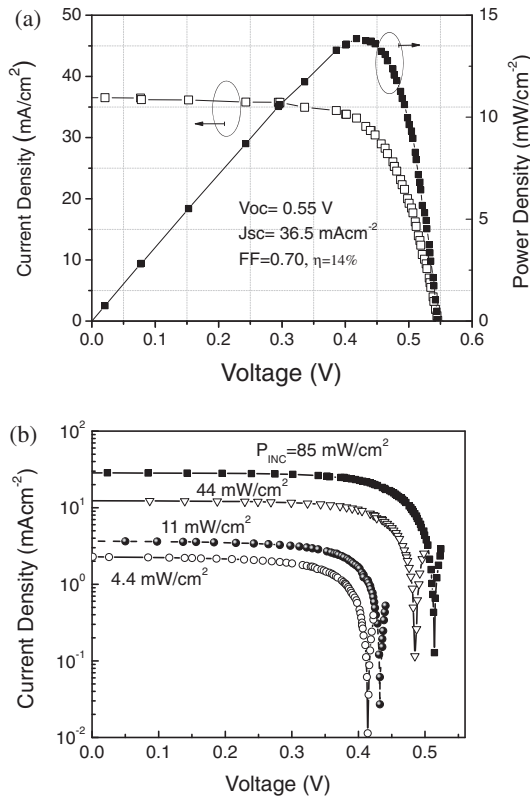


Fig. 3. (a) J - V characteristics and P - V curve of CIGS solar cell under AM1.5 illumination; (b) J - V curves measured under different incident light power densities.

shown in Fig. 3(a). The testing device has a surface area of $\sim 0.04 \text{ cm}^2$. The V_{oc} , J_{sc} , and FF are directly extracted from illuminated J - V curve. The J - V relationship can be described as³¹⁾

$$J = J_0 \left\{ \exp \left[\frac{q}{AkT} (V - JR_s) \right] - 1 \right\} + \frac{V - JR_s}{R_{SH}} - J_{ph}, \quad (2)$$

where J_0 is reverse saturation current density, A is ideality factor. Although Eq. (2) is implicit and non-solvable analytically, and many algorithms have been proposed to approximately extract the device parameters. In this paper, we used Sites's³²⁾ method to determine J_0 , A , R_s , and R_{SH} . By assuming J_{ph} is constant and ignoring 1 in the parentheses, Eq. (2) can be simplified as

$$1 = J_0 \exp \left[\frac{q(V - JR_s)}{AkT} \right] \times \frac{\frac{dV}{dJ} - R_s}{AkT} + \frac{\frac{dV}{dJ} - R_s}{R_{SH}}. \quad (3)$$

By substituting Eq. (2) in Eq. (3), rearranging both sides and assuming $R_s \ll R_{SH}$ we can get

$$\frac{dV}{dJ} = R_s + \frac{AkT}{q} \frac{1 - \frac{1}{R_{SH}} \frac{dV}{dJ}}{J + J_{ph} - \frac{V}{R_{SH}}}. \quad (4)$$

R_{SH} is determined from slope at J_{sc} in J - V curve. By plotting dV/dJ vs $(1 - R_{SH}dV/dJ)/(J + J_{ph} - V/R_{SH})$ in forward bias region, shown in Fig. 4, R_s and A therefore can be extracted. Arranging Eq. (1) again, we can get

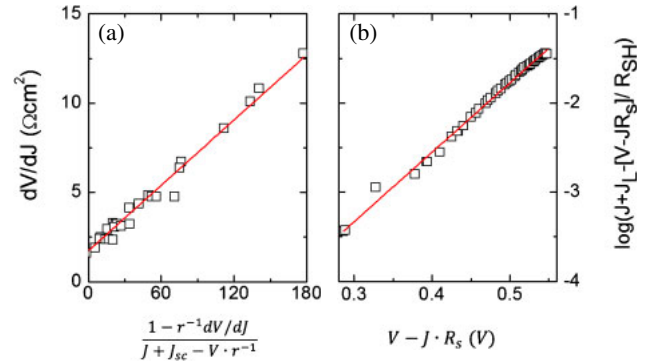


Fig. 4. (Color online) (a) dV/dJ vs $(1 - R_{SH}dV/dJ)/(J + J_{ph} - V/R_{SH})$ plots in forward bias region shows $A = 2.34$, $R_s = 1.74 \Omega$; (b) $\log[J + J_{ph} - (V - JR_s)/R_{SH}]$ vs $(V - JR_s)$ plots in forward bias region shows $J_0 = 2.19 \times 10^{-3} \text{ mA/cm}^2$, $A = 2.16$.

$$\log \left(J + J_{ph} - \frac{V - JR_s}{R_{SH}} \right) = \log J_0 + \frac{\log e}{AkT} (V - JR_s). \quad (5)$$

By plotting $\log[J + J_{ph} - (V - JR_s)/R_{SH}]$ vs $(V - JR_s)$ near forward bias region, shown in Fig. 4, J_0 and A can be extracted. By comparing ideality factor A values extracted by two methods, we can conclude that both results are consistent with each other. The best performance for our solar cells tested is: $\eta = 13.9\%$, $V_{oc} = 0.55 \text{ V}$, $J_{sc} = 36.55 \text{ mA/cm}^2$, $FF = 0.7$, $R_s = 1.74 \Omega \text{ cm}^2$, $R_{SH} = 866 \Omega \text{ cm}^2$, and $J_0 = 2.19 \times 10^{-3} \text{ mA/cm}^2$. The experimental results agree well with the modeling results: $\eta = 14.3\%$, $V_{oc} = 0.58 \text{ V}$, $J_{sc} = 30.0 \text{ mA/cm}^2$, $FF = 0.84$, without doing any extensive optimization of the device parameters used in this calculation. The similarity between both results indicates that simulation of CIGS is accurate and used materials parameters can be used in optimization and design of flexible CIGS photovoltaic cells. Figure 3(b) shows J - V curves under different incident light power densities. With the increase of incident light power density, J_{sc} and V_{oc} increase. As it was described before,²⁶⁾ under a given incident light power density (\mathfrak{S}), J_{sc} can be expressed as

$$J_{sc}(\mathfrak{S}) = \frac{P_{inc}(\mathfrak{S})}{P_{inc}} \times J_{ph} = k \times J_{ph}, \quad (6)$$

where J_{ph} is the short circuit density under 100 mW/cm^2 of standard AM1.5 irradiation, $k = P_{inc}(\mathfrak{S})/P_{inc}$, where P_{inc} is the standard incident light power density of 100 mW/cm^2 , and $P_{inc}(\mathfrak{S})$ denotes the incident light power density of a standard incident light P_{inc} filtered by a filter of transmittance \mathfrak{S} , namely when $\mathfrak{S} = 40\%$, $P_{inc} = 100 \text{ mW/cm}^2$, then $P_{inc}(\mathfrak{S}) = 40 \text{ mW/cm}^2$. And for V_{oc} , we have

$$V_{oc} = \frac{Ak_B T}{q} \ln \left(\frac{J_{sc}}{J_0} + 1 \right). \quad (7)$$

By substituting Eq. (6) into Eq. (7), V_{oc} under a given incident light intensity can be derived as

$$V_{oc} = \frac{Ak_B T}{q} \ln \left(k \cdot \frac{J_{ph}}{J_0} + 1 \right). \quad (8)$$

The calculated data based on Eqs. (6) and (8) fit well with experiment results.²⁸⁾ This result indicates, as expected, that

Table II. Performance of CIGS solar cells of different cell areas.

Area (cm ²)	FF	J _{sc} (mA cm ⁻²)	V _{oc} (V)	η (%)	R _s (Ω cm ²)	R _{SH} (Ω cm ²)
0.04	0.69	35.00 ± 0.7	0.55 ± 0.005	13.3	2.0	534
0.16	0.47	32.06 ± 0.6	0.51 ± 0.004	7.68	7.4	459
0.25	0.42	29.86 ± 0.7	0.49 ± 0.005	6.14	10.2	117
1.00	0.27	14.02 ± 0.7	0.46 ± 0.006	1.74	35.2	41

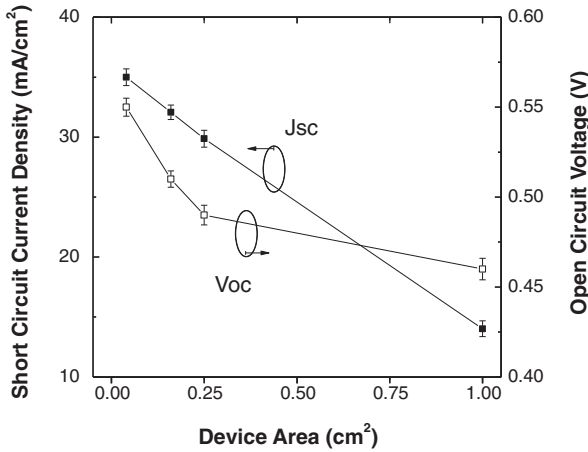


Fig. 5. Measured short circuit current density (J_{sc}) and open circuit voltage (V_{oc}) for different size devices.

a fluctuation of light intensity may cause a large change of current output in a series connected solar cell module while its voltage output is relatively stable.

Table II shows performance of the CIGS solar cells with different device areas. We observed that J_{sc} and V_{oc} decreases with an increasing area of the solar cell, Fig. 5. This can be associated with the impact of R_s and R_{SH} on device performance. For short circuit condition, $V = 0$, from Eq. (2) we have:

$$J = J_0 \left[\exp\left(\frac{q}{AkT} (-JR_s)\right) - 1 \right] - \frac{JR_s}{R_{SH}} - J_{ph}. \quad (9)$$

Since $J_0 \ll J_{ph}$, we get

$$J_{sc} \approx -\frac{JR_s}{R_{SH}} - J_{ph}, \quad (10)$$

that is

$$J_{sc} \approx \left| \frac{-J_{ph}}{1 + R_s G_{SH}} \right| = \frac{|J_{ph}|}{1 + R_s G_{SH}}, \quad (11)$$

where $G_{SH} = 1/R_{SH}$. Since $R_s \cdot G_{SH}$ increases with the increasing of device area, J_{sc} will decrease. Therefore J_{sc} decreases with the increasing of device area. For open circuit condition, $J = 0$, from Eq. (2) we have

$$V_{oc} = \frac{Ak_B T}{q} \ln\left(\frac{J_{ph}}{J_0} + 1 - \frac{V_{oc} \cdot G_{SH}}{J_0}\right). \quad (12)$$

Obviously, when G_{SH} increases, V_{oc} decreases, which is consistent with the experiment results shown in Fig. 5. Moreover, larger area device shows a lower FF and external efficiency. With the increasing of device area, R_s increases while R_{SH} is reduced. Both these parameters will affect device FF and solar cell efficiencies. Hence these results

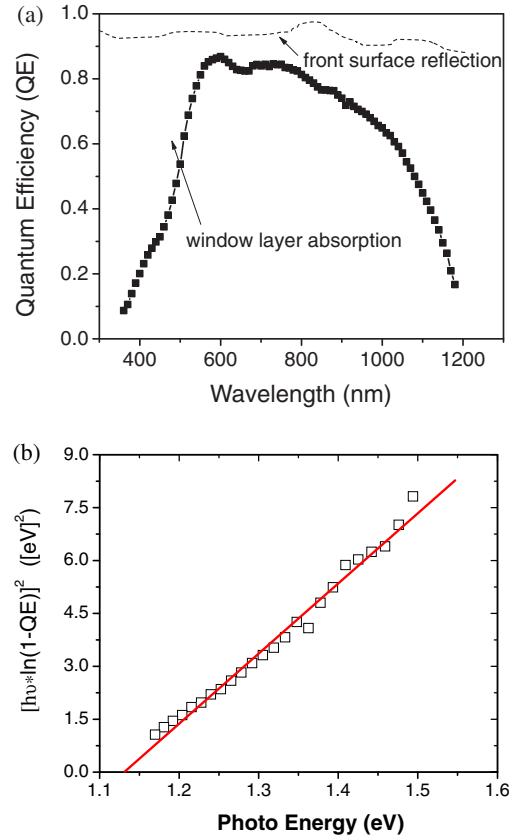


Fig. 6. (Color online) (a) Measured EQE curve for 13.9% efficient flexible CIGS solar cell; (b) $[hv \cdot \ln(1 - QE)]^2$ vs hv plot is shown.

indicate that for a large area solar cell, reducing the series resistance is critical to achieve a high efficiency. Therefore, as expected, for larger area devices metal grids must be used to maintain higher device efficiency. However, their design must be optimized for optimum device operation.

Figure 6(a) shows external quantum efficiency (EQE) result for our 13.9% efficient solar cell. The EQE is as high as 90% at peak and remains no less than 40% QE for $\lambda > 1100$ nm. EQE drops very quickly from ~ 520 (corresponding to CdS bandgap of 2.42 eV) to 300 nm. Light absorption in CdS layer and ZnO window layer can contribute to this decrease. The sunlight is first absorbed by the window and buffer layer. Usually these materials have a high bandgap: ZnO ~ 3.3 eV and CdS ~ 2.42 eV. The light with a short wavelength, namely below 550 nm, is partially absorbed by the CdS film. Therefore, as expected, poorer quantum efficiency at shorter wavelength is observed. Reduction of the CdS thickness is expected to reduce this absorption loss and increase device output current. However, usually a thicker CdS film is needed to compensate for SS substrate roughness. Hence compromise must be reached between absorption loss and impact of substrate roughness on device performance. Also CIGS absorption coefficient and QE decreases with the increasing photon wavelength. Since at longer wavelength the photo-generated carrier diffusion length is shorter, the not fully optimized CIGS absorber film thickness has direct impact on reduced carrier collection efficiency in the range of 900 to 1100 nm. The free carrier absorption of the TCO film at longer wavelength will also contribute to reduction of EQE.

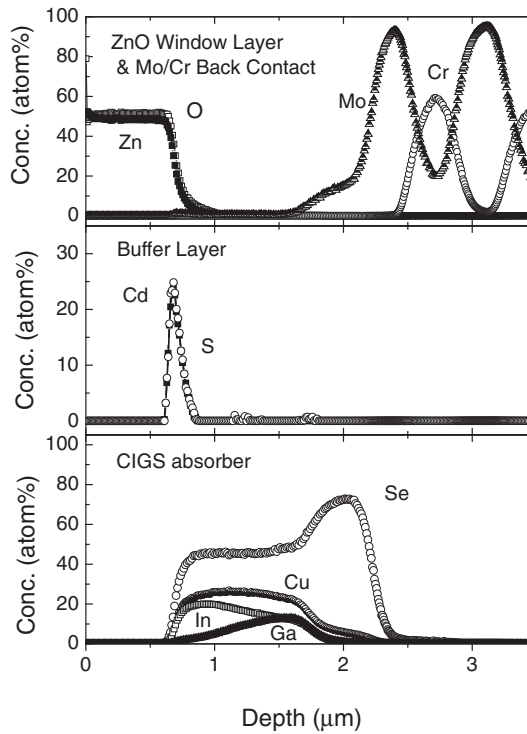


Fig. 7. SIMS depth profile of element Cu, In, Ga, Se, S, Cd, Zn, O, Mo, Cr concentration through the device is shown.

The general internal quantum efficiency (IQE) is defined as $IQE = EQE / (1 - \text{reflectance})$. For CIGS, IQE can be approximated as³³⁾

$$IQE \equiv 1 - \frac{e^{-\alpha W}}{\alpha L + 1}, \quad (13)$$

where α , W , and L are absorption coefficient, depletion width, and minority carrier diffusion length, respectively. By assuming $\alpha L \ll 1$, the equation is simplified as

$$IQE = 1 - e^{-\alpha W}. \quad (14)$$

Absorption efficient can be described by

$$\alpha = \frac{\ln(1 - IQE)}{W}. \quad (15)$$

Since the absorption coefficient and energy bandgap for direct bandgap (E_g) material has a relationship as: $(\alpha \cdot hv)^2 \propto hv - E_g$, E_g can be extrapolated by plotting $[hv \cdot \ln(1 - IQE)]^2$ vs hv .³⁴⁾ This plot is shown in Fig. 6(b) indicating that the CIGS bandgap is ~ 1.13 eV.

3.3 Physic-chemical characterization

Figure 7 shows the SIMS depth profile through our CIGS solar cell device. The studied structure of ZnO/CdS/CIGS/MoSe₂/Mo/Cr/Mo/Cr/SS can be divided into four layers: MoSe₂/Mo/Cr/Mo/Cr back contact and barrier layer, CIGS absorber, CdS buffer layer and ZnO window layer. Bright field TEM (BF-TEM) images, Fig. 8, indicate the thickness of each film.

3.3.1 Back contact and barrier layer

Different from a typical CIGS-based solar cell structure,⁵⁾ Fig. 8 shows that our device has stacked Cr/Mo/Cr/Mo

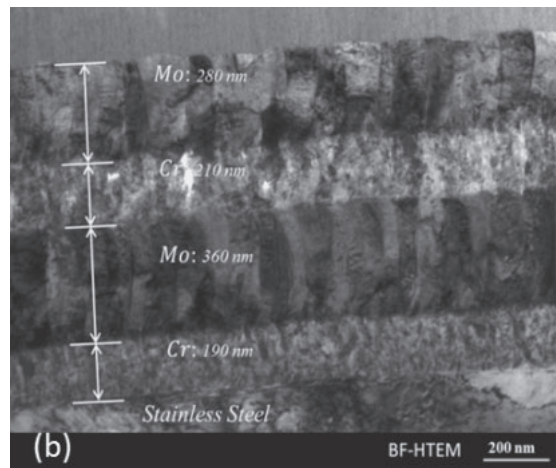
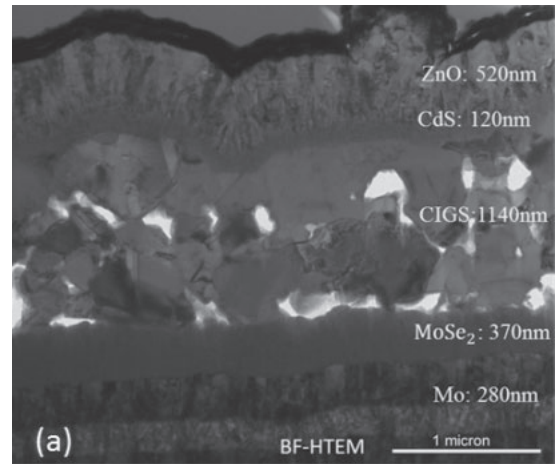


Fig. 8. (a) BF-TEM cross-section image of device shows a structure of ZnO/CdS/CIGS/MoSe₂/Mo/Cr; (b) BF-TEM cross-section image of Mo/Cr/Mo/Cr/SS back contact and barrier layer.

double layers between SS and CIGS absorber as a back contact layer. The base thin Cr layer of thickness ~ 190 nm is designed to improve adhesion of films over SS substrate. Chromium oxide is found on the surface of the SS³⁵⁾ and generally Cr sticks to its own oxide better than other metals promoting Cr adhesion to SS. Moreover, Cr is a fairly good barrier to Fe diffusion from the SS substrate at high temperature. Due to the roughness of SS substrates, some peaks may penetrate the base of thin Cr film so that another layer of Cr is added to help block Fe diffusion from higher peaks being present on the SS surface. Figure 9 shows SIMS profiles for Fe, Cr, and Ni metallic impurities in CIGS layer. The data for referenced clean CIGS solar cell grown on glass substrates is also include in this figure. We can observe that Fe and Ni ions concentrations are much lower than reference while Cr concentration value is slightly higher than the reference sample. Herz et al.³⁶⁾ have investigated effect of Al₂O₃ film between SS substrate and Mo back contact as a barrier layer for blocking the metallic impurities diffusion from SS substrate. For the device without a barrier layer they obtained for both Fe and Cr 10^{-2} at. % in CIGS layer. The concentration values were reduced to the level of 10^{-4} at. % when a 3- μ m-thick Al₂O₃ barrier layer was added. From Fig. 9 we can see that the Fe concentration in our device with Cr/Mo layers is at

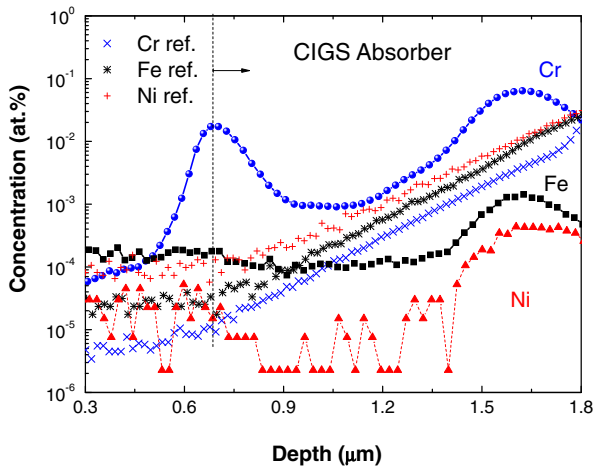


Fig. 9. (Color online) Measured SIMS depth profile of metallic impurities, Ni, Fe, and Cr distribution in the device and reference data are shown.

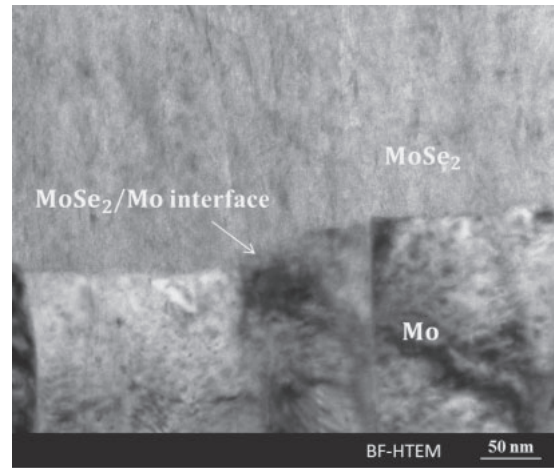


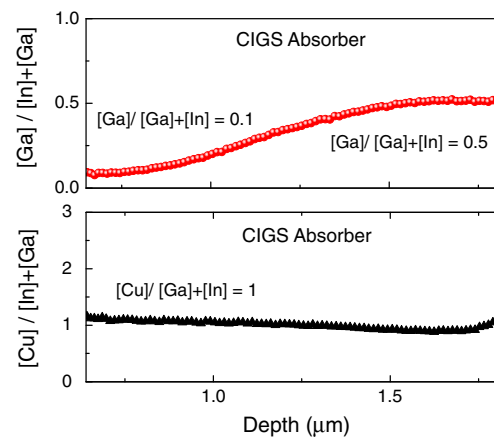
Fig. 10. BF-TEM image of MoSe₂/Mo interface.

the level of 10⁻⁴ at. % indicating that the Cr/Mo layers successfully blocked Fe diffusion into CIGS absorber from SS substrate. Also our results showed that our proposed solution is equivalent to deposition of a 3-μm-thick Al₂O₃ barrier layer. The measured Cr concentration in CIGS layer is two orders of magnitudes higher than Fe, which indicates that this Mo/Cr structure may introduce some Cr impurities into CIGS absorber. It is common agreement that iron presence in CIGS will harm the device performance. No negative effect of Cr on device performance has ever been reported. Therefore, we can conclude that the design of double Cr/Mo barrier layers blocks quite well possible diffusion of harmful iron ions from SS substrate into CIGS absorber, and enhances overall the device performance.

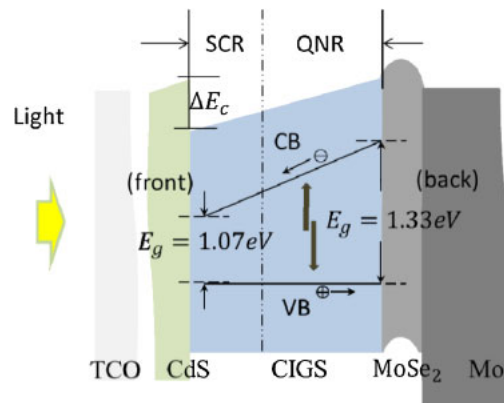
From SIMS data shown in Fig. 7, we can also observe that near the bottom of CIGS layer there is formation of a layer having [Mo]/[Se] ~ 1 : 2, which can be associated with the MoSe₂ layer. This layer results from diffusion and reaction of Se with Mo back contact layer.³⁷⁾ Figure 10 shows the BF-TEM image of the MoSe₂ film and the interface between MoSe₂ and Mo layers. In agreement with Shiro Nishiwaki and others,^{26,37)} MoSe₂ layer helps in electrons collection by forming a good metal-semiconductor contact and reducing electrons (minor carriers) recombination at the back contact interface.

3.3.2 Absorber

From data shown in Fig. 7, we can observe composition variation of gallium alloy in the CIGS layer: gallium concentration is low near the surface but high at the bottom, while indium accumulated at the surface. Figure 11(a) shows calculated [Ga]/([In] + [Ga]) profile from the front to back indicating a normal grading structure.³⁸⁾ At front, [Ga]/([In] + [Ga]) ratio has a value of ~0.1 and linearly increase up to ~0.5 towards the bottom. Knowing that band gap of CIGS depends on gallium composition:³¹⁾ $E_g^{CIGS}(x) = E_g^{CIS}(1-x) + xE_g^{CGS}$, where $E_g^{CIS} = 1.01$ eV and $E_g^{CGS} = 1.65$ eV, we can calculate the bandgap grading profile in CIGS. Since Ga alloy does not influence valance band (VB),



(a)



(b)

Fig. 11. (Color online) (a) Cu–In–Ga composition grading profile in CIGS layer; (b) Schematic of normal band grading profile in CIGS layer is shown.

the conduction band (CB) of CIGS increases linearly with Ga alloy concentration producing a bandgap change of +0.26 eV from front to back interface with an initial and final bandgap of 1.07 and 1.33 eV, respectively, Fig. 11(b). The electron photo-excited into conduction band will have a tendency to “roll down” by the electrostatic potential. The force acting on photo-generated electrons coming from

additional quasi-electric field will “push” electrons toward space charge region (SCR) and reduce recombination at the back contact interface. Hence minority carrier collection in this region will enhance photocurrent output. Although there are still debates among researchers on how much the additional quasi-electric field built into CIGS (due to band grading) can enhance short circuit current, it has been a common conclusion that the open circuit voltage mainly depends on the bandgap in SCR.³⁹⁾ Here, the lowest bandgap of 1.07 eV at front ($E_{g,front}$), induced by In accumulation on CIGS surface, is responsible for limited open circuit voltage (0.55 V). Estimated bandgap of absorber calculated from QE data (~ 1.13 eV), close to $E_{g,front}$, also supports the idea that the low bandgap material present on top dominates in the CIGS layer.

Other effect that we can observe in Fig. 7 is that the In diffuses to the top surface and Ga diffuses to MoSe₂/film surface during selenization process. This will result in CuInSe₂ (CIS) phase located near top surface and CuGaSe₂ (CGS) phase located near MoSe₂/film interface. The segregation of CIS and CGS may be due to the difference in surface free energies. Marudachalam et al.⁴⁰⁾ proposed that CIS may have a much lower surface free energy than the CGS, therefore there will be a tendency for the CIS phase segregated towards the top surface. Another explanation can be related to the difference in the reaction rates between the two phases. Selenization of Cu–Ga precursor to form CGS needs more time or high temperature than reaction of Cu–In with Se to form CIS. Besides, when In:CuGa is co-sputtered on the heated substrate the In is melting. During CIGS film formation, the nature metallurgy comes into play and Cu and Ga are more compatible with each other than either is with indium. Molten In islands were found on the top surface which can also lead to In accumulation after Se vapor selenization.

Figure 12 shows the SEM image of cross section of CIGS/CdS/ZnO layers. We can clearly see columnar CIGS grains with a grain size of ~ 400 nm. Also many nano-scale voids are observed through the CIGS layer. From the BF-TEM images, Figs. 8(a) and 13, we find that most “big” voids are located in two lines, one at bottom film/MoSe₂ interface and another in the middle of CIGS layer. Shafarman et al.⁴¹⁾ also observed voids which were located at the bottom. They explained their formation by Cu₉Ga₄ dissolving into CIS as the film is reacted. As indicated in Fig. 13, most voids have a triangle shape. Lei et al.³⁷⁾ proposed a model based on the Kirkendal effect to explain these triangle voids formation. The interdiffusion and phase reaction in the bilayer process are responsible for voids forming in polycrystalline CIGS. We make use of this model to explain the formation mechanism of those intergranular voids (in the middle of film) observed in our device. First, solid phase diffusion usually occurs by one of three mechanisms: (1) atomic interchange by a ring mechanism, (2) the migration through interstitial sites, or (3) via vacant sites. The primary mechanism in CIGS is believed to be via vacancies.^{40,42)} When an atom moves by a vacancy mechanism either another atom or a vacancy must move in the opposite direction. When vacancies are the opposite flux, they accumulate within the solid beyond its solid solubility and precipitate as Kirkendal voids. This can be considered as

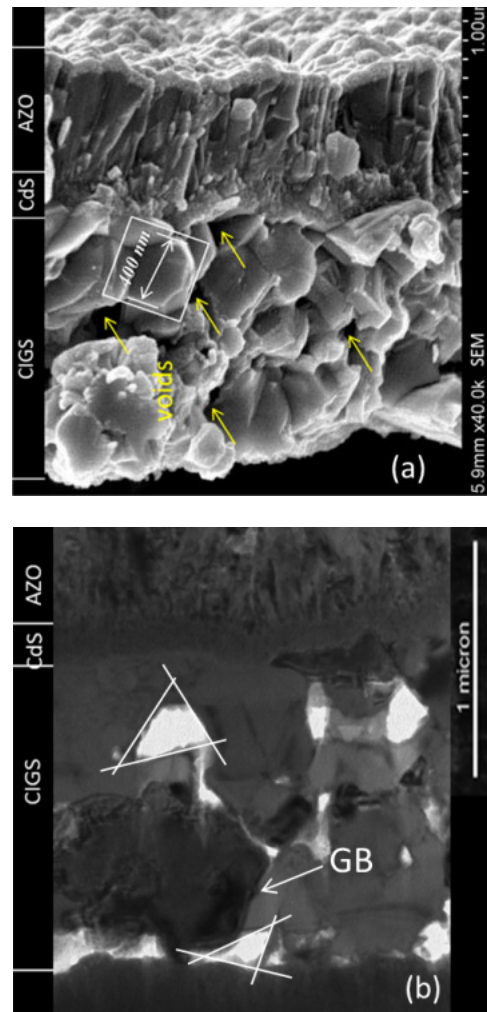


Fig. 12. (Color online) (a) SEM cross section image of CIGS/CdS/AZO layers shows clearly columnar grains, with grain size of ~ 400 nm as well as many nano-scale voids indicated by yellow arrows; (b) BF-TEM cross-section image of CIGS layer shows voids in the film having a triangle shape.

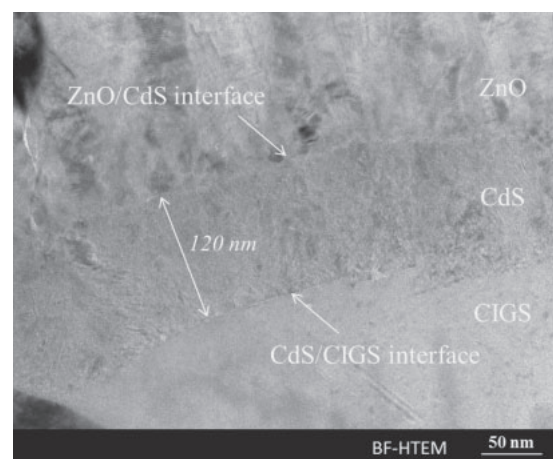


Fig. 13. BF-TEM image of CIGS/CdS/AZO interfaces.

the origin of the voids formation. Since the diffusion rates of Cu, In, and Ga are different, where Cu usually has a diffusion rate two orders larger than In and Ga, CuSe_x would diffuse quickly into InSe/Ga₂Se₃ with a counter flux of vacancies into initially Cu-rich region. The $[Cu]/([In] + [Ga])$ ratio at

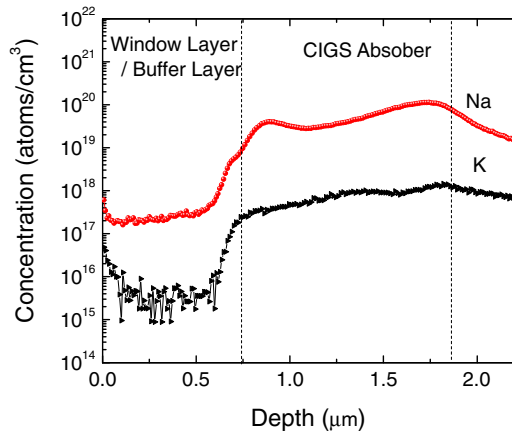


Fig. 14. (Color online) SIMS depth profile of elements Na and K concentration in the device is shown.

bottom of CIGS layer, shown in Fig. 11(a), is observed to increase over ~ 1.0 in support of the idea that CuSe_x diffuses faster into (In,Ga) than In,Ga diffusions into Cu-rich region. This would lead to Kirkendal voids throughout the film but mainly located at initially Cu-rich region. This agrees well with the observation that intergranular voids are mostly located in the middle of film where initially Cu-rich region was present. In conclusion, we believe that the intergranular voids in our device are induced by the interdiffusion of Cu and In/Ga when CuSe_x reacts with $\text{InSe}/\text{Ga}_2\text{Se}_3$ to form CIGS during the selenization process. The direct impact of these voids on device performance is not clear. We might speculate that these voids have reduced the effective thickness of the absorber which can introduce photocurrent loss due to the insufficient light absorption; this is especially true for relatively long wavelength light.

3.3.3 Window layer

From images in Fig. 8(a), we can see that CdS layer is thick enough to compensate for the roughness of the SS substrate surface. Figure 13 shows a high resolution image of interface between CdS and CIGS films. CdS layer has a thickness of ~ 120 nm. As we discussed in Sect. 3.2.1, a somehow thinner CdS film would expect to reduce the losses of photo excited current in the window layer and improve overall device efficiency. But at the same time thinner film will not be very effective in smoothing SS substrate surface roughness. Further optimizations of CdS thickness and reduction of SS roughness could improve device overall performance.

3.3.4 Sodium and potassium incorporation

Sodium (Na) and potassium (K) incorporations in CIGS layer are shown in Fig. 14. It has been widely accepted that the Na in CIGS absorber plays a role of CIGS grain boundaries passivation leading to improved solar cell performance.⁴³⁾ Our observation is also consistent with this conclusion. From Fig. 14 we can conclude that the Na distribution mainly concentrates at two terminals of CIGS layer, where grain boundary density is the highest. Moreover, we would like to propose an additional explanation of the sodium positive impact on CIGS solar cell device performance. O. Lundberg et al.⁴⁴⁾ reported an experiment

on In and Ga diffusion with/without sodium incorporation. His experiment results indicated that the interdiffusion of In and Ga is higher in layers grown without any presence of sodium producing an uniform distribution of In and Ga along depth. Lee et al.⁴⁵⁾ also reported that their CIGS solar cell fabricated on a non-soda-lime glass (SLG) glass without an additional Na incorporation showed an uniform distribution of In and Ga along depth. In our device, with additional sodium incorporation, Fig. 11(a), we observed clearly Ga/In grading profile along depth. This might indicate that the interdiffusion of In and Ga is prohibited because of the presence of Na in CIGS layer. Rockett et al.⁴⁶⁾ reported similar results of graded Ga/In profile with Na incorporation. Therefore, we would like to conclude that the presence of sodium in CIGS will impede the interdiffusion of In and Ga so that enable the graded band profile formation. This graded band profile enhances electrons collection which improves the device overall performance.

To our surprise in SIMS spectra, the element K profile was also present, although we did not intend to introduce such element. Rudmann reported similar results⁴³⁾ and speculated that the presence of K profile is due to the mass interferences in SIMS analysis where $^{23}\text{Na}^{+16}\text{O}$ has the same nominal mass as the analyzed ^{39}K ion. This is usually called isobaric effect. In our analytical mode mass spectrometer has sufficient mass resolution that can separate atomic ions from molecular ion interferences. Moreover, to exclude this isobaric effect, the measured material composition was calibrated by RBS. During the RBS analysis, high-energy (MeV) He^{2+} ions are directed onto the sample then the energy distribution and yield of the backscattered He^{2+} ions at a given angle is measured. Since the backscattering cross section for each element is known, it is accurate to obtain a quantitative compositional depth profile from the RBS spectrum. In this analytical mode, the Na^{+}O mass interference is not significant. Therefore, we would like to indicate that our measured potassium profile is real. But we currently do not know from where the potassium comes from? Since we are using SS substrate, the K atmos could not be associated with its out-diffusion from substrate such as SLG substrate. More study is needed to elucidate this interesting phenomenon.

4. Conclusions

In this work, we evaluated CIGS solar cell fabricated on flexible SS substrate by the low cost mass production roll-to-roll process based on co-sputtering approach. Band grading and voids are observed in CIGS layer. Their formation mechanisms have been discussed as well as their expected influence on solar cell performance. By adjusting bandgap of CIGS in space charge region, we can expect a higher output open circuit voltage resulting in higher efficiency. We have also shown that device simulation results are consistent with the experimental data. Therefore, simulation tool used in this work can be very useful in the design and optimization of the CIGS solar cells structure before their fabrication. This will allow very fast and cost effective design of the CIGS solar cells with the optimized optoelectronic properties.

In the future it would be desirable to try to adjust band grading profile of CIGS absorber to achieve a larger open circuit voltage. It is also important to have a full under-

standing of voids formation mechanism in CIGS layer by metallic precursor-selenization process and their impact on device performance. More advanced simulation models should be evaluated, namely band grading effect should be included in the simulation, for device design and performance optimization. Moreover, the stability properties of CIGS flexible solar cell under humidity environment are also need to be carefully studied.

Acknowledgements

The authors gratefully acknowledge Dr. Yan, Baojie of United Solar Ovonic for his assistance with the solar cells measurements. Dr. Y. G. Xiao of Crosslight, Inc. is also acknowledged for his support with the APSYS software. The authors also acknowledge Jeff Mayer of Evans Analysis Group for his help in all chemical analysis described in this paper.

- 1) M. Kaelin, D. Rudmann, and A. N. Tiwari: *Sol. Energy* **77** (2004) 749.
- 2) K. L. Chopra, P. D. Paulson, and V. Dutta: *Prog. Photovoltaics* **12** (2004) 69.
- 3) M. Grätzel: *Nature* **414** (2001) 338.
- 4) J. C. Bernède: *J. Chil. Chem. Soc.* **53** (2008) 1549.
- 5) I. Repins, M. Contreras, M. Romero, Y. Yan, W. Metzger, J. Li, S. Johnston, B. Egaas, C. DeHart, and J. Scharf: *Prog. Photovoltaics* **19** (2011) 84.
- 6) B. M. Başol, V. K. Kapur, C. R. Leidholm, A. Halani, and K. Gledhill: *Sol. Energy Mater. Sol. Cells* **43** (1996) 93.
- 7) S. Ishizuka, H. Hommoto, N. Kido, K. Hashimoto, A. Yamada, and S. Niki: *Appl. Phys. Express* **1** (2008) 092303.
- 8) T. Yagioka and T. Nakada: *Appl. Phys. Express* **2** (2009) 072201.
- 9) M. S. Kim, J. H. Yun, K. H. Yoon, and B. T. Ahn: *Solid State Phenom.* **124–126** (2007) 73.
- 10) D. Herrmann, F. Kessler, K. Herz, M. Powalla, A. Schulz, J. Schneider, and U. Schumacher: *MRS Proc.* **763** (2003) B6.10.1.
- 11) D. Rudmann, D. Brémaud, A. F. da Cunha, G. Bilger, A. Strohm, M. Kaelin, H. Zogg, and A. N. Tiwari: *Thin Solid Films* **480–481** (2005) 55.
- 12) R. Caballero, C. A. Kaufmann, T. Eisenbarth, T. Unold, R. Klenk, and H.-W. Schock: *Prog. Photovoltaics* **19** (2011) 547.
- 13) A. Chirilă, S. Buecheler, F. Pianezzi, P. Bloesch, C. Gretener, A. R. Uhl, C. Fella, L. Kranz, J. Perrenoud, S. Seyrling, R. Verma, S. Nishiwaki, Y. E. Romanyuk, G. Bilger, and A. N. Tiwari: *Nat. Mater.* **10** (2011) 857.
- 14) Y. Hashimoto, T. Satoh, S. Shimikawa, and T. Negami: Proc. 3rd World Conf. Photovoltaic Energy Conversion, 2003, 2LN-C-09.
- 15) S. Wiedeman, M. E. Beck, R. Butcher, I. Repins, N. Gomez, B. Joshi, R. G. Wendt, and J. S. Britt: *Proc. 29th IEEE Photovoltaic Specialists Conf.*, 2002, p. 575.
- 16) M. E. Beck, S. Wiedeman, R. Huntington, J. VanAlsburg, E. Kanto, R. Butcher, and J. S. Britt: *Proc. 31st IEEE Photovoltaic Specialists Conf.*, 2005, p. 211.
- 17) N. G. Dhere, S. R. Ghongadi, M. B. Pandit, A. H. Jahagirdar, and D. Scheiman: *Prog. Photovoltaics* **10** (2002) 407.
- 18) V. K. Kapur, A. Bansal, P. Le, O. Asensio, and N. Shigeoka: Proc. 3rd World Conf. Photovoltaic Energy Conversion, 2003, 2P-D3-43.
- 19) J. Klaer, J. Bruns, R. Henninger, K. Topper, R. Klenk, K. Ellmer, and D. Braunig: Proc. 2nd World Conf. Photovoltaic Solar Energy Conversion, 1998, p. 537.
- 20) D. R. Hollars, R. Dorn, P. D. Paulson, J. Titus, and R. Z. Miasolé: *MRS Proc.* **865** (2005) 3199.
- 21) S. Michael, A. D. Bates, and M. S. Green: *Proc. 31st IEEE Photovoltaic Specialist Conf.*, 2005, p. 719.
- 22) R. Stangl, C. Leendertz, and J. Haschke: in *Solar Energy*, ed. R. D. Rugecu (InTech, Rijeka, 2010) Chap. 14, p. 319.
- 23) Z. Q. Li, Y. G. Xiao, M. Lestrade, and Z. M. S. Li: *Proc. 33rd IEEE Photovoltaic Specialists Conf.*, 2008, p. 1.
- 24) Y. G. Xiao, Z. Q. Li, M. Lestrade, and Z. M. S. Li: *Proc. SPIE* **7771** (2010) 77710K.
- 25) N. B. Kindig and W. E. Spicer: *Phys. Rev.* **138** (1965) A561.
- 26) W. N. Shafarman, S. Siebentritt, and L. Stolt: *Handbook of Photovoltaic Science and Engineering* (Wiley, New York, 2011) 2nd ed., Chap. 13.
- 27) S. A. Al Kuhaimi: *Sol. Energy Mater. Sol. Cells* **52** (1998) 69.
- 28) R. Zhang, D. R. Hollars, and J. Kanicki: Proc. 19th Int. Workshop AM-FPD'12, 2012, p. 289.
- 29) T. Minemoto, Y. Hashimoto, T. Satoh, T. Negami, H. Takakura, and Y. Hamakawa: *J. Appl. Phys.* **89** (2001) 8327.
- 30) A. Yamada, K. Matsubara, K. Sakurai, S. Ishizuka, H. Tampo, H. Shibata, T. Baba, Y. Kimura, S. Nakamura, H. Nakanishi, and S. Niki: *MRS Proc.* **865** (2005) F5.19.1.
- 31) W. Wang: Dr. Thesis, Chemistry Engineering, Oregon State University (2012).
- 32) J. R. Sites and P. H. Mauk: *Sol. Cells* **27** (1989) 411.
- 33) S. S. Hegedus and W. N. Shafarman: *Prog. Photovoltaics* **12** (2004) 155.
- 34) Q. Cao, O. Gunawan, M. Copel, K. B. Reuter, S. J. Chey, V. R. Deline, and D. B. Mitzi: *Adv. Energy Mater.* **1** (2011) 845.
- 35) K. Nomura and Y. Ujihira: *J. Mater. Sci.* **25** (1990) 1745.
- 36) K. Herz, A. Eicke, F. Kessler, R. Wächter, and M. Powalla: *Thin Solid Films* **431–432** (2003) 392.
- 37) C. Lei, A. Rockett, I. M. Robertson, W. N. Shafarman, and M. Beck: *J. Appl. Phys.* **100** (2006) 073518.
- 38) R. Ortega-Borges and D. Lincot: *J. Electrochem. Soc.* **140** (1993) 3464.
- 39) T. Dullweber, G. Hanna, W. Shams-Kolahi, A. Schwartzlander, M. A. Contreras, R. Noufi, and H. W. Schock: *Thin Solid Films* **361–362** (2000) 478.
- 40) M. Marudachalam, R. W. Birkmire, H. Hichri, J. M. Schultz, A. Swartzlander, and M. M. Al-Jassim: *J. Appl. Phys.* **82** (1997) 2896.
- 41) K. Kim, G. M. Harket, T. Huynh, and W. N. Shafarman: *J. Appl. Phys.* **111** (2012) 083710.
- 42) D. J. Schroeder, G. D. Berry, and A. A. Rockett: *Appl. Phys. Lett.* **69** (1996) 4068.
- 43) D. Rudmann: Dr. Thesis, Swiss Federal Institute of Technology (ETH) (2004).
- 44) O. Lundberg, J. Lu, A. Rockett, M. Edoff, and L. Stolt: *J. Phys. Chem. Solids* **64** (2003) 1499.
- 45) J. W. Lee, C. H. Choi, K. H. Kang, M. J. Shin, S. H. Kwon, and J. H. Yun: *J. Korean Phys. Soc.* **60** (2012) 1997.
- 46) A. Rockett, J. S. Britt, T. Gillespie, C. Marshall, M. M. Al Jassim, F. Hasoon, R. Matson, and B. Basol: *Thin Solid Films* **372** (2000) 212.